Structural and chemical properties of a $c(2\times2)$-Ti/Pt(100) second-layer alloy: A probe of strong ligand effects on surface Pt atoms

Shuchen Hsieh, Taketoshi Matsumoto, Matthias Batzill,* and Bruce E. Koel†
Department of Chemistry, University of Southern California, Los Angeles, California 90089-0482, USA
(Received 25 March 2003; published 20 November 2003)

We investigated the structure and chemisorption properties of a Ti/Pt(100) surface alloy using Auger electron spectroscopy (AES), low energy electron diffraction (LEED), scanning tunneling microscopy (STM), x-ray photoelectron spectroscopy (XPS), x-ray photoelectron diffraction (XPD), low-energy alkali ion scattering (ALISS), and temperature programed desorption (TPD). Samples were prepared by evaporating Ti onto a clean hex-Pt(100) reconstructed surface at 300 K. After annealing the sample to 800 K, a $c(2\times2)$ LEED pattern was observed that sharpened as the temperature was increased to 920 K. Further annealing to 1000 K caused this (2×2) LEED pattern to become diffuse because of the onset of disorder in the surface layers resulting from Ti diffusion into the bulk. Using XPD and ALISS, we determined that this LEED pattern is due to an ordered alloy structure that has Ti atoms present in the second layer of a $c(2\times2)$-Ti/Pt(100) surface alloy, and not in the topmost layer. Thus, the surface layer of this alloy is pure Pt. XPS showed that the Ti $2p$ peak from the surface alloy is shifted by 1.4 eV to higher binding energy than that of a thick Ti film, and the Pt $4f$ peak is shifted by 0.1 eV higher from that of the clean hex-Pt(100) reconstructed surface, consistent with the formation of strong intermetallic bonds upon alloying. The chemisorption properties of the surface alloy were probed using CO and H_2 adsorption. CO adsorbed reversibly on the alloy, desorbing in TPD in a broad peak with a maximum at 376 K. This is lower by 132 K from the CO desorption peak from a clean Pt(100) surface. Thermal desorption of H_2 showed a similar peak shift to lower temperature, and much less hydrogen (20%) adsorbed on the $c(2\times2)$-Ti/Pt(100) alloy than on Pt(100). These results show that second layer Ti atoms exert a strong ''ligand'' or electronic effect on Pt atoms at the surface. Thus, the $c(2\times2)$-Ti/Pt(100) surface alloy represents an interesting model system for studying ligand effects on the chemistry of a bimetallic alloy surface.

DOI: 10.1103/PhysRevB.68.205417 PACS number(s): 68.47.De, 82.45.Jn, 82.65.+r

INTRODUCTION

The catalytic properties of dispersed transition metals supported on titanium dioxide (TiO_2) are of interest because of their importance as heterogeneous catalysts. Early on, for the group VIII metals (Fe, Ni, Rh, Pt, Pd, and Ir) supported on TiO_2, it was observed that the amount of CO and H_2 that chemisorbed under high-temperature reducing conditions was significantly diminished.[1] This effect was termed ''strong metal-support interaction'' (SMSI), and it is reversible during a reduction-oxidation cycle.[2]

Several models have been proposed to account for this reduced chemisorption activity. Migration of cationic TiO_x particles onto the top of Pt crystallites could act as site blocking agents and thereby reduce the number of available chemisorption sites.[3] A second model, proposed by Beard and Ross,[4] involved Ti diffusion into Pt particles to form a Ti/Pt alloy leading to the altered chemical behavior of the catalyst. Tauster *et al.*[2] strengthened this argument by showing that alloying is thermodynamically possible under high-temperature reducing conditions associated with SMSI conditions. Formation of Pt_3Ti is highly exothermic $(-81.7$ kcal/mol),[5] and this has been attributed to strong binding interactions between d orbitals of the two metals. Furthermore, Brewer *et al.*[6] stated that d-orbital bonding between the metals would be expected to change the adsorption properties of the Pt atoms.

Platinum-titanium alloys are of interest as a model system for studying SMSI effects on Pt/TiO_2 catalysts, but also for their structural characteristics and use in electronic materials. Early work on the (111) and (100) crystal faces of bulk Pt_3Ti single crystals was performed using low energy electron diffraction (LEED) and Auger electron spectroscopy (AES).[7,8] Bardi *et al.*[9] used AES and dynamical LEED-intensity calculations to conclude that the (100) surface of a bulk Pt_3Ti crystal forms a $c(2\times2)$ structure with the outermost layer composed of a one-to-one ratio of Ti and Pt. In this model, the second layer is 100% Pt. Alternatively, several other groups more recently have proposed that the $Pt_3Ti(100)$ surface layer is composed of pure Pt. For example, Atrei *et al.*[10] proposed a Pt-terminated $Pt_3Ti(100)$ surface layer based on dynamical LEED data. Chen *et al.*[11] agreed, postulating further that deeper layers alternated between (100) layers of pure Pt and a $c(2\times2)$-Ti/Pt(100) structure. Paul *et al.*[12] also assigned a pure-Pt surface layer to a bulk $Pt_3Ti(111)$ sample using angle-resolved x-ray photoelectron spectroscopy (ARXPS), and the same model was proposed in a separate study of core-level binding energy shifts.[13]

In the present paper, we report on the structural and chemical properties of a $c(2\times2)$-Ti/Pt(100) surface alloy formed by depositing a Ti film on Pt(100) and annealing to 920 K. In a related study, the alloying behavior of Ti deposited on a Pt(111) substrate was studied by Ringler *et al.*[14] using scanning tunneling microscopy (STM) and synchrotron-source XPS, but the issue of surface composition was not addressed. In our study, Ti atoms were found to

be present only in the second atomic layer. The chemical properties of this $c(2\times2)$-Ti/Pt(100) surface alloy were probed using CO and H_2 temperature programed desorption (TPD). Lower desorption temperatures for both CO and H_2 on the alloy indicate a reduced reactivity compared to the clean Pt(100) surface. Since this alloy has a pure-Pt surface layer, this change in reactivity is clearly due to a "ligand" effect exerted by Ti atoms in the second layer and thus provides a model system for understanding such effects.

EXPERIMENTAL METHODS

STM experiments were performed in an ultrahigh vacuum (UHV) chamber described in detail elsewhere.[15] The chamber was equipped with a double-pass cylindrical mirror analyzer (CMA) for AES, rear-view LEED optics, quadrupole mass spectrometer for residual gas analysis and TPD, ion-gun for sample cleaning, electron beam-heated Ti-evaporation source, and precision leak valves for gas dosing, including a one directed-beam gas doser for H_2. The STM was a home-built single-piezo tube following the design of Mugele and co-workers.[16] Electrochemically etched polycrystalline-tungsten tips were used in all experiments. STM images were obtained in constant current mode with the bias voltage applied to the tip. For AES, the incident electron energy was 3 keV and the modulation voltage used to record spectra in $dN(E)/dE$ mode was 6 eV. The sample was heated using electron bombardment from the backside of the crystal, and the sample temperature was measured with a chromel/alumel thermocouple spot welded directly to the side of the crystal.

Low-energy ion scattering (LEIS), XPS, and x-ray photoelectron diffraction (XPD) experiments were performed in a second UHV chamber that is described in detail elsewhere.[17] The chamber was equipped with a Colutron ion gun providing a collimated, monoenergetic ion source for LEIS and alkali ion scattering spectroscopy (ALISS), ion sputter gun, dual-anode x-ray source for XPS and XPD, and a Perkin-Elmer Model 10-360 spherical capacitor analyzer (SCA) with a multichannel detector. Various ports were available for metal evaporators and gas dosers. Binding energies (BE's) in XPS were defined relative to the Pt $4f_{7/2}$ peak at 71.7 eV BE on clean Pt(100).

The manipulator had three translational (x, y, and z axes) and two rotational (polar and azimuthal) degrees of freedom. Rotational motion was controlled by stepper motors either manually or using a computer interface. The accuracy of the polar angle (ψ for XPD and Ψ for ALISS), azimuth angle ϕ, and scattering angle θ were $\pm0.5°$, $\pm1°$, and $\pm0.5°$, respectively. All XPD and ALISS measurements reported in this paper were taken on the ordered $c(2\times2)$-Ti/Pt(100) surface alloy prepared as described below.

XPD results presented here use a polar angle ψ defined with respect to the surface normal, that is, $\psi=0°$ corresponds to the analyzer located perpendicular to the surface plane. The angle between the energy analyzer and x-ray source was fixed at 42.5°. An Al-$K\alpha$ x-ray source operating at 300 W (15 kV) was used with SCA pass energies of 187.85 and 23.5 eV for XPD and XPS, respectively. Pt $4f$ and Ti $2p$ core-level peak intensities used in XPD were obtained from integration of peak areas after background subtraction.

For ALISS measurements, an incident Li^+-ion beam of 1.0 keV energy at 0.6 nA beam current to the sample was used. This condition insured that no detectable changes occurred in ALISS spectra over the time required to obtain them. The SCA was operated at 1127.1-eV pass energy. A complete energy scan could be acquired every 60 s and a complete polar angle scan could be obtained in 90 min. The angle between the SCA and ion source was fixed at 36° to give a scattering angle of 144°. Conventionally in ALISS, the polar angle Ψ is defined with respect to the crystal surface plane, with $\Psi=90°$ corresponding to ions incident perpendicular to the surface. ALISS polar scans were obtained for $\Psi=0$ to 95°. An energy scan was obtained at every polar angle for $E_{\text{scattering}}/E_{\text{incident}}=0.4$ to 0.9, which fully covers the scattering peaks for both Pt and Ti. The Pt and Ti scattering signal intensity was obtained from integration of the single-scattering peaks after background subtraction. A linear background subtraction procedure was used where the endpoints were chosen by averaging 10 data points in each wing of the peak.

The Pt(100) single crystal (Atomergic, $5N$ purity) was cleaned using standard procedures consisting of cycles of 500-eV Ar^+-ion sputtering followed by annealing in a background of 2×10^{-7}-Torr O_2 at 1000 K, with a final annealing in UHV at 1200 K. The cleanliness of the sample was monitored by AES and LEED, and the procedure was repeated until no contamination of the surface could be detected. The background pressure in both vacuum chambers was below 4×10^{-10} Torr. An electron-beam heated titanium rod was used to deposit Ti films onto the Pt substrate. The sample was annealed (as described below) immediately after Ti deposition in order to reduce contamination, e.g., by CO and H_2O. While the Ti deposition rate and coverage were not determined explicitly, we found that a well-ordered $c(2\times2)$-Ti/Pt(100) surface alloy was formed reproducibly if an AES peak-to-peak ratio of Ti(387)/Pt(237)=1.5 was observed after depositing the Ti film and annealing to 920 K. A Ti deposition time of 30 s was used usually to achieve this. All of the data reported herein was obtained from surfaces prepared in this way.

RESULTS

A. Ti deposition and alloy formation on the Pt(100)-hex surface

Vapor deposition of clean Ti films is complicated by the problem of the high reactivity and oxidation of Ti by residual gases in the chamber. We used a sample preparation procedure optimized to form well-ordered, oxygen-free bimetallic surfaces. Once the Pt(100)-hex surface was clean, as determined by AES and a sharp (5×20) LEED pattern, Ti was deposited and the Pt substrate was immediately annealed to 920 K without performing AES to determine the Ti coverage. This minimized exposure of the sample to contaminant gases and produced an oxygen-free surface within the detection limits of AES. We sometimes observed a weak (3×5)

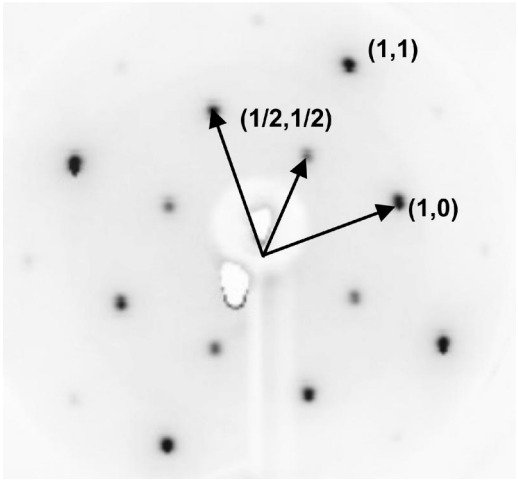

FIG. 1. LEED image showing a $c(2\times2)$ pattern obtained after depositing an ultrathin film of Ti on Pt(100) and annealing to 920 K for 10 s ($E_i=124$ eV).

LEED pattern that we attribute to TiO_x-overlayer formation,[18] although no oxygen was detected using AES in some cases. Thus, LEED was a sensitive probe of the cleanliness of the bimetallic surface. Annealing the clean Ti film on Pt(100) to 920 K causes formation of a $c(2\times2)$ LEED pattern, as shown in Fig. 1. AES spectra as presented in Fig. 2 indicated that the best conditions for producing the $c(2\times2)$-Ti/Pt(100) structure was a Ti(387)/Pt(237) AES peak-to-peak ratio of about 1.5. Depositing additional Ti also gave a Ti/Pt ratio of 1.5 after annealing, with excess Ti diffusing into the bulk of the crystal. For example, on a sample prepared with an ''as-deposited'' Ti/Pt AES ratio of 5.0, annealing caused this ratio to decrease to 1.5. This indicates that either extensive 3D clustering of Ti or interdiffusion and subsurface alloying had occured. Alloying would be expected given the large exothermicity associated with forming Ti-Pt bonds, but we carried out ALISS and XPD studies in order to unambiguously confirm this interpretation and determine the location of Ti atoms among the top several layers of the substrate.

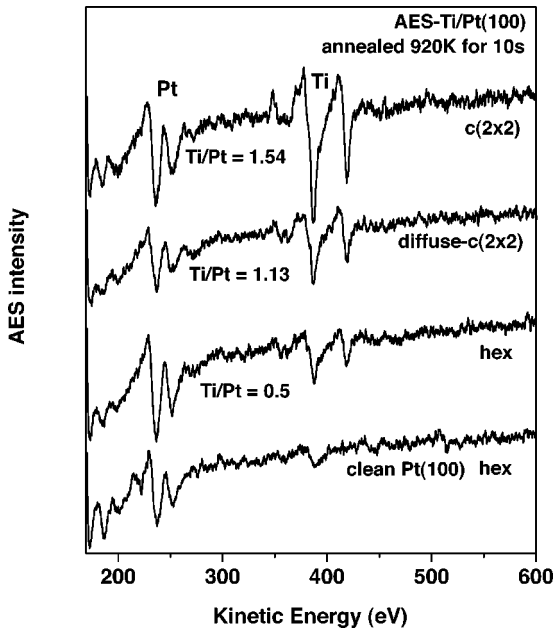

FIG. 2. AES spectra following annealing various Ti films deposited on Pt(100). Surfaces were all annealed to 920 K for 10 s prior to collecting the spectra. A Ti/Pt AES peak-to-peak ratio of about 1.5 gave the best $c(2\times2)$ pattern in LEED and surfaces with this ratio were used in all subsequent experiments. Depositing excess Ti also yielded a Ti/Pt AES ratio of 1.5 after annealing, with the additional Ti diffusing into the bulk of the crystal.

B. Structure of the Ti/Pt(100)-$c(2\times2)$ surface

1. STM

STM was used to image the real-space structure of the $c(2\times2)$-Ti/Pt(100) surface. The sample was cooled to room temperature prior to scanning in each experiment and LEED was used to confirm the long-range $c(2\times2)$ ordering. A large-scale scan (50×50 nm^2) of the surface is shown in Fig. 3(a). The overall surface morphology in this region has two distinct levels: (i) bright, square islands (10–50 nm on a side) that are one atomic layer high and (ii) the darker area that surrounds them. Additionally, a number of dark spots can be seen in the brighter areas that may be due to vacancies or chemical contamination. The islands, as shown in Fig. 3(a), tend to form with edges along the [110] azimuths.[19] This is different from the behavior observed on a Sn/Pt(100) surface alloy where islands form along [100] directions.[20] In general, dense-packed step edges usually have the lowest free energy,[21] and therefore, a surface composed of pure Pt would tend to form step edges along [110] directions. Alternatively, a bimetallic $c(2\times2)$ alloy can achieve a more energetically favorable structure by forming islands with step edges along [100] azimuths because the lower free energy element can terminate the steps. This was observed in the case of a $c(2\times2)$-Sn/Pt(100) surface alloy where step edges were terminated by Sn atoms along the [100] azimuths.[20]

Figure 3(b) shows a small-scale scan (10×10 nm^2) of an island similar to those shown in Fig. 3(a). Periodic rows were observed that are separated by approximately 4 Å. This corresponds to the distance between Pt atoms along the [100] azimuth for a (1×1)-Pt(100) surface (3.92 Å). (Rows along the [010] direction were not observed, but this could be due to a poor tip that gives better resolution along the rapid scanning direction.) This result is confirmed by the known orientation of the sample, and when combined with the island-edge orientation in Fig. 3(a), can be used to support a model of an alloy surface that has a pure-Pt top layer with subsurface Ti.

2. XPS

Figure 4 shows XPS spectra of the Ti $2p$ region for a Ti/Pt(100) alloy and a thick Ti film deposited on Pt(100). Within the short time (5 min) required for the XPS scan, there was no detectable oxygen contamination of the thick films. The Ti $2p_{3/2}$ peak from the alloy occurred at 456.2 eV, which is shifted by $+1.4$ eV BE relative to that from the

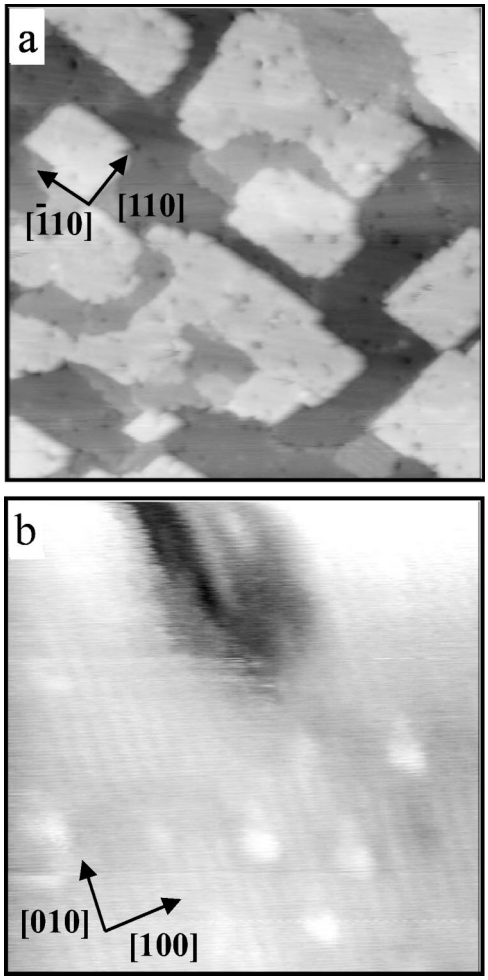

FIG. 3. STM topographical images of a $c(2\times2)$-Ti/Pt(100) surface that was annealed at 920 K for 10 s and cooled to room temperature prior to scanning. (a) 50.2×50.2 nm^2 image showing large (5–10 nm) square islands. Dark spots in these islands and the layer below might be due to oxidized Ti atoms or clusters. (b) 10×10 nm^2 image. Rows along the [100] direction are separated by approximately 4 Å, in good agreement with an expected value of 3.93 Å for dimensions on Pt(100). The tunneling conditions for the image in (a) were $U_{\text{bias}}=+330$ mV, $I=+1.26$ nA, and for the image in (b) were $U_{\text{bias}}=+42.4$ mV, $I=+2.24$ nA.

thick Ti film. At a more surface sensitive take-off angle of 34° with respect to the surface plane, as shown in Fig. 5, the Pt $4f_{7/2}$ peak was also shifted 0.1 eV to higher binding energy relative to that for the clean Pt surface. These results are consistent with Ringler's study[14] of Ti on Pt(111) in which the Ti $2p$ peak was shifted by 1.5 eV toward higher binding energy compared to pure Ti. Also, Chen *et al.*[22] showed that the Ti $2p$ and Pt $4f$ core levels were shifted 1.3 and 0.4 eV, respectively, for the $Pt_3Ti(111)$ surface compared to the pure, single-component metals.

3. XPD

Figure 6 shows a schematic representation of the [100] and [110] azimuthal cross sections for a fcc(100)-oriented

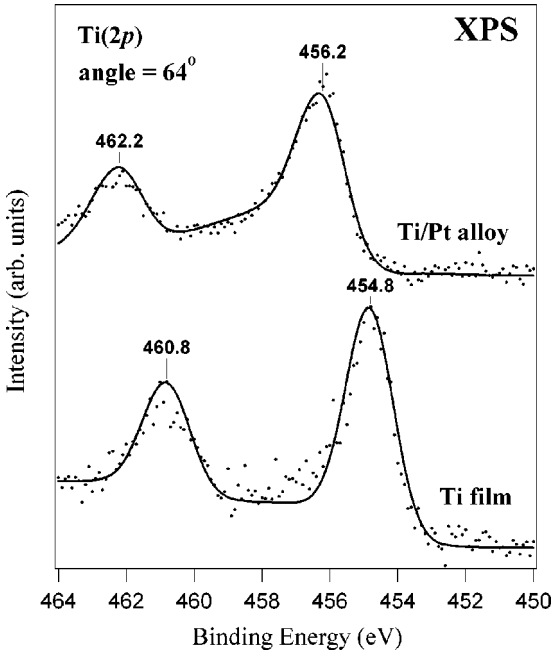

FIG. 4. XPS spectra of the Ti $2p$ region for the Ti/Pt(100) alloy and for a thick Ti film on Pt(100), at a take-off angle of 64° with respect to the surface plane. The Ti $2p_{3/2}$ peak at 456.4 eV from the alloy (upper trace) is shifted by 1.4 eV to higher binding energy relative to that from a thick Ti film (lower trace).

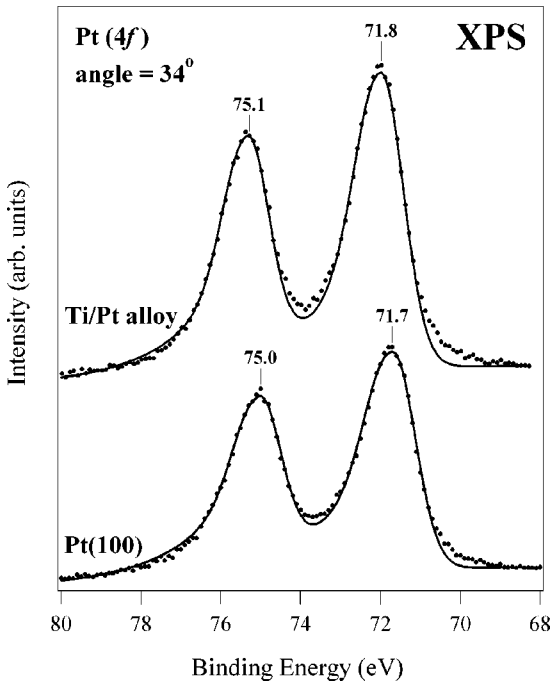

FIG. 5. XPS spectra of the Pt $4f$ region for the Ti/Pt(100) alloy and for a thick Ti film on Pt(100), at a more glancing take-off angle of 34° with respect to the surface plane. The Pt $4f_{7/2}$ peak from the alloy is shifted by 0.1 eV to higher binding energy relative to that from clean Pt.

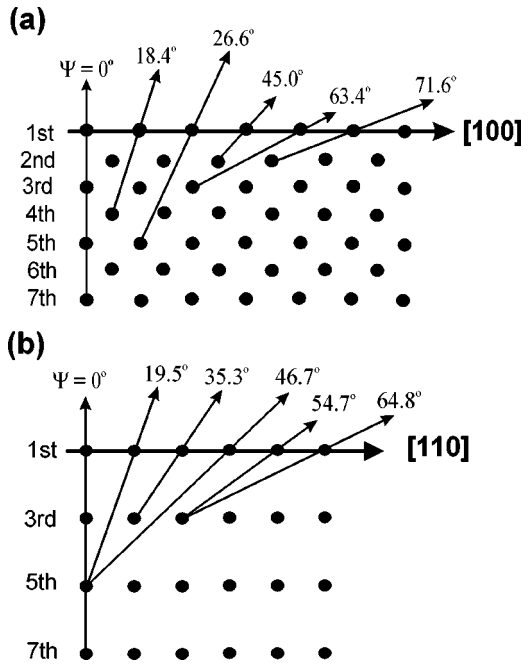

FIG. 6. Cross-sectional view of an fcc(100) crystal along the [100] (a) and [110] (b) azimuthal directions, showing the origin of the forward focusing peaks observed in XPD. The polar angle ψ is defined with respect to the surface normal.

crystal. Arrows indicate directions that are expected to show forward-scattering enhancements for XPD from the Pt(100) crystal.

XPD spectra for the clean (1×1)-Pt(100) and $c(2\times2)$-Ti/Pt(100) surfaces are shown in Figs. 7 and 8 along the [100] and [110] azimuths, respectively. Pt $4f$ and Ti $2p$ XPD spectra were obtained by integration of both of the Pt $4f_{7/2}$ and $4f_{5/2}$ and Ti $2p_{3/2}$ and $2p_{1/2}$ peaks, respectively. The Pt scans in Figs. 7(a) and 8(a) were obtained from a clean (1×1)-Pt(100) surface prepared by lifting the (5×20)-Pt(100) reconstruction using NO adsorption immediately followed by H_2 exposure to remove residual adsorbed oxygen.[23]

XPD polar scans along the [100] azimuth are shown in Fig. 7. The Pt $4f$ polar scan in Fig. 7(a) for a pure (1×1)-Pt(100) surface shows forward-scattering features near those angles predicted at $\psi=45.0°$ and 71.6° from second layer atoms, $\psi=0$ and 63.4° from third layer atoms, and $\psi=18.4°$ from the fourth atomic layers (see Fig. 6). In Fig. 8(a) for a Pt $4f$ polar scan along the [110] azimuth from a pure (1×1)-Pt(100) surface, we expect to see forward scattering features at $\psi=0°$, 35.3°, and 54.7° from third layer atoms. Apart from a general decrease in intensity at high angles which complicates observation, some of the peaks in Figs. 7(a) and 8(a) are shifted from the expected polar angle positions. This could be due to failure to remove all of the hex-Pt(100) reconstruction or misalignment of the sample along the azimuthal direction during set up or precession during a polar scan. The primary features that we are interested in for determining surface structure concern those corresponding to the shortest internuclear distances where theory predicts the strongest diffraction effects.

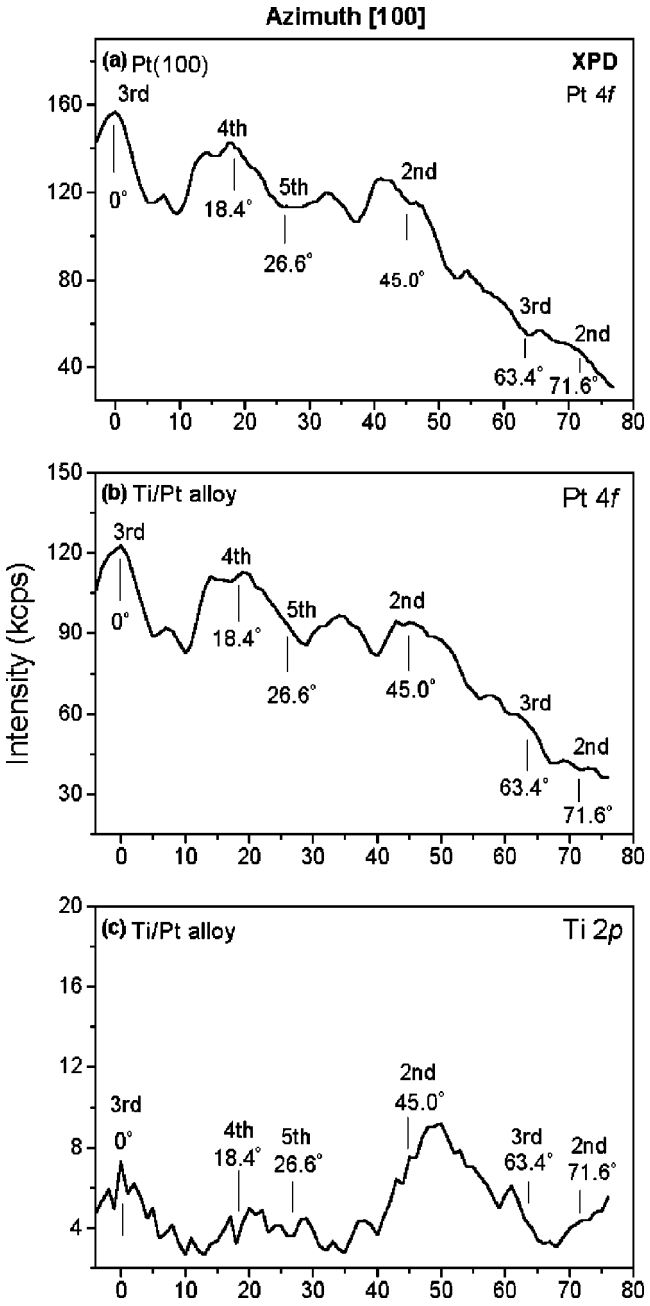

FIG. 7. XPD polar scans along the [100] azimuth obtained from (a) clean (1×1)-Pt(100) substrate, and (b) and (c) $c(2\times2)$-Ti/Pt(100) alloy. Directions that are expected to show forward-scattering enhancements for XPD from the Pt(100) crystal are also included. The Pt $4f$ polar scan in (b) shows forward focusing diffraction peaks consistent with that in (a). (c) A peak at 50° along the [100] direction, indicating that Ti is present in the second layer.

The Pt $4f$ polar scans of the Ti/Pt alloy surface in Figs. 7(b) and 8(b) closely resemble the corresponding scans in Figs. 7(a) and 8(a). However, the peaks for the alloy are shifted to higher polar angles, which could occur if relaxation decreased the interlayer distances near the surface. For example, if the distance between the first and second layers

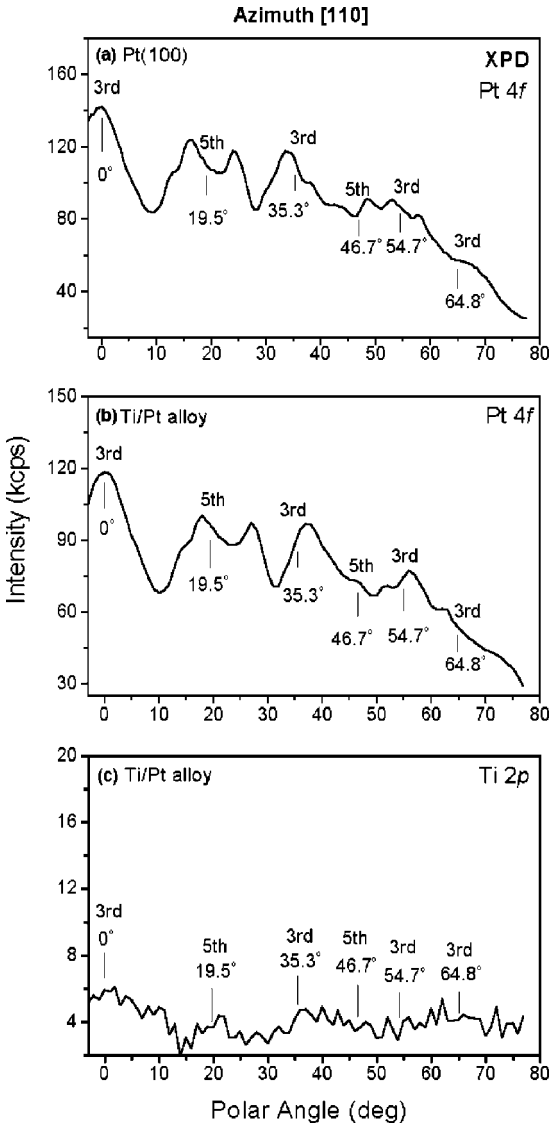

FIG. 8. XPD polar scans along the [110] azimuth obtained from (a) clean (1×1)-Pt(100) substrate, and (b) and (c) $c(2\times2)$-Ti/Pt(100) alloy. Directions that are expected to show forward-scattering enhancements for XPD from the Pt(100) crystal are also included. The Pt $4f$ polar scan in (b) shows forward focusing diffraction peaks consistent with that in (a). No enhancement of the Ti peak is observed along the [110] azimuthal direction.

and the second and third layers was each reduced by 5%, then the third-layer peak in the [110] direction would shift $+3.4°$ and the second-layer peak in the [100] direction would shift $+0.8°$.

Figures 7(c) and 8(c) show the Ti $2p$ polar scans of the alloy. Figure 7(c) shows a clear enhancement near 50° which confirms that Ti is present in the second layer. The shift of this peak to a polar angle larger than 45° can be explained by relaxation as described above and possibly additional local relaxations due to the strong Ti-Pt interaction. The absence of any appreciable enhancements at other angles indicates that no other deeper layers contain a substantial Ti concentration.

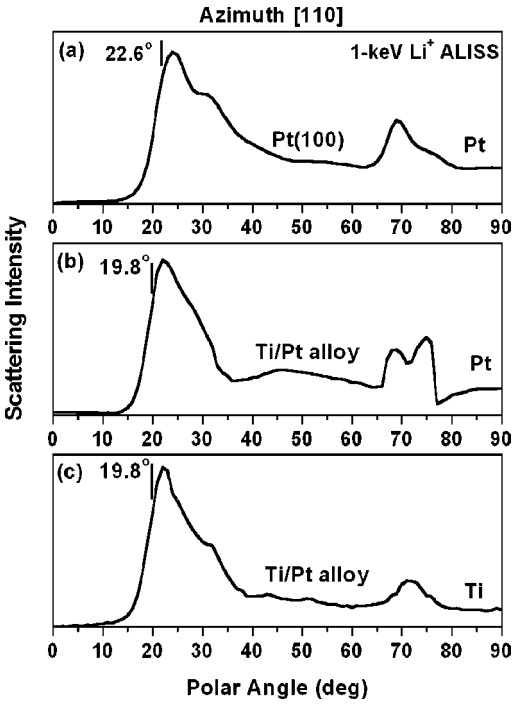

FIG. 9. ALISS Li^+-Pt polar angle scans along [110] azimuth from (a) clean (1×1)-Pt(100) substrate, and (b) $c(2\times2)$-Ti/Pt(100) alloy. Fig. (c) shows a Li^+-Ti polar angle scan along the [110] azimuth for the alloy. The critical angle Ψ is calculated at 90% of the enhancement peak maximum.

4. Li^+*-ISS*

Figures 9 and 10 show polar-angle ALISS scans for Pt and Ti using 1-keV Li^+ ions scattered from the $c(2\times2)$-Ti/Pt(100) surface along the [110] and [100] azimuths, respectively. The critical angle indicated in each figure Ψ_c is taken as the angle which gives 90% of the maximum intensity of the enhanced scattering peak.[24–26] Figures 9(a) and 10(a), included for comparison, are ISS spectra of a clean (1×1)-Pt(100) surface from a previous study.[26] The critical angle of the scattering peak from first-layer Pt along the [110] azimuth in Fig. 9(a) is 22.6°, which is higher than that along the [100] azimuth of 18.9° shown in Fig. 10(a). This is due to the smaller interatomic spacing along the [110] direction than along the [100] direction, thus a higher polar angle is required to bring the first layer Pt atoms out of the ''shadow cone'' created by their preceding neighbors. Shadow cones are regions that are parabolic in shape that form behind each surface atom within which incident ions cannot penetrate and thus neighboring atoms are ''shadowed'' from scattering incident ions (and thus cannot contribute a signal) for certain incident directions.[25,27,28] Peaks at near 20° are related to scattering from first layer atoms, and those near 70° correspond to scattering from atoms in the second layer. In Fig. 9(b), we observe a double peak feature at near 70°. This has been described by Niehus and Comsa,[29,30] as originating from second-layer atoms that create a ''blocking cone'' focusing effect, i.e., outgoing ions form a blocking cone as they leave the surface. There are several notable features observed in ALISS spectra of the

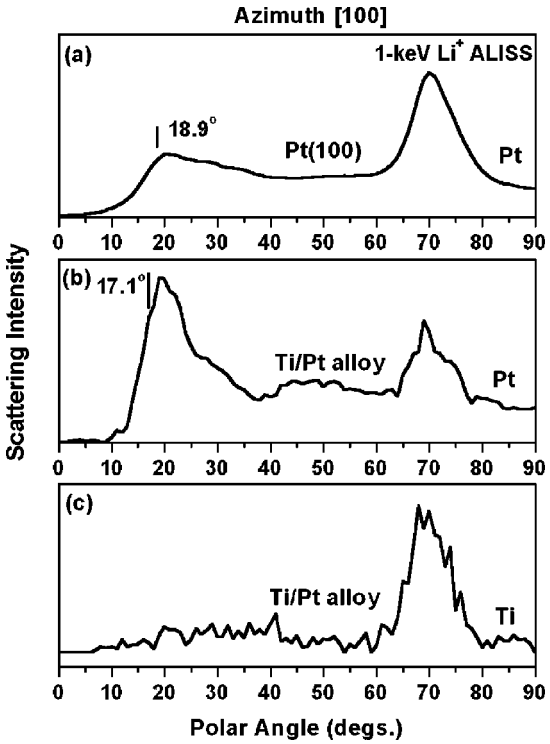

FIG. 10. ALISS Li^+-Pt polar angle scans along the [100] azimuth from (a) clean (1×1)-Pt(100) substrate, and (b) $c(2\times2)$-Ti/Pt(100) alloy. Fig. (c) shows a Li^+-Ti polar angle scan along the [100] azimuth for the alloy. The absence of a Ti peak at low incident angles indicates that there is no Ti present in the surface layer. The Ti peak observed at a higher incident angle is consistent with Ti atoms present in the second layer and is consistent with the conclusion reached from XPD.

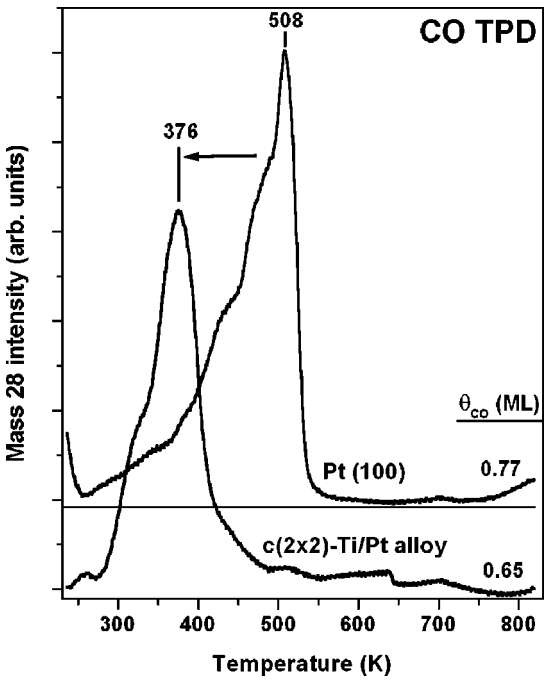

FIG. 11. CO TPD curves following a 6-L CO exposure on a clean Pt(100) surface (top) and on a $c(2\times2)$-Ti/Pt(100) surface alloy (bottom). The CO desorption peak maximum shifted lower by 132 K, from 508 K on Pt(100) to 376 K on the Pt-Ti alloy.

$c(2\times2)$-Ti/Pt(100) alloy: (i) scans in both Figs. 9(b) and 9(c) have low critical angles at 19.8° compared to 22.6° for a clean (1×1)-Pt(100) surface in Fig. 9(a), (ii) along the [100] azimuth, the critical angle for Pt scattering in Fig. 10(b) for the alloy is 17.1°, (iii) the Pt scattering intensity at 70° in Fig. 10(b) is about one-half the intensity of that at 20°, and (iv) in Fig. 10(c), no low angle, Ti-scattering peak is observed; however, a peak occurs at a high scattering angle of 70°. From these results, we conclude that there is no Ti in the first layer, but there is a significant amount of Ti in the second layer. This issue will be addressed further in the Discussion section below.

C. CO and H_2 adsorption on the Ti/Pt(100)-$c(2\times2)$ surface

Temperature programed desorption (TPD) of CO and H_2 were used to probe the effects of alloying on the surface reactivity of the $c(2\times2)$-Ti/Pt(100) alloy. TPD experiments were carried out using a heating rate of 5 K/s with the QMS ionizer in line of sight with the sample surface. The sample was situated 1 cm away from a small entrance aperture to a shield that surrounded the mass spectrometer which minimizes contributions from the back and edges of the crystal.

1. CO TPD

Thermal desorption spectra for CO are presented in Fig. 11 that were taken following a 6-L CO dose on both a clean Pt(100)-hex surface and on a $c(2\times2)$-Ti/Pt(100) surface alloy. In previous ALISS (Ref. 26) studies, it was shown that a 6-L CO exposure saturated the Pt(100) surface and the coverage was defined as $\theta_{CO}=0.77$ ML.[23] In this study, the CO desorption peak maximum for the most strongly bound CO was shifted down by 132 K for the alloy compared to pure Pt(100), i.e., from 508 to 376 K. The integrated peak area for CO desorption (which is proportional to the CO coverage) is only 15% less for the alloy than for the clean Pt(100) surface. In addition, CO TPD features from the alloy are quite similar to those for CO on clean Pt(100), where CO bonds at fourfold bridge and atop sites. Using Redhead[31] analysis and assuming first-order desorption kinetics and a constant preexponential factor of 1×10^{13} s^{-1}, the desorption activation energies were estimated to be 23 kcal/mol for the $c(2\times2)$-Ti/Pt(100) surface and 31.4 kcal/mol for clean Pt(100). This result for clean Pt(100) is consistent with previous studies by Panja *et al.*,[32] Thiel *et al.*,[33] and Barteau *et al.*[34] that reported adsorption energies of 32.3, 33.1, and 32.6 kcal/mol, respectively.

2. H_2 TPD

Figure 12 shows H_2 thermal desorption spectra following a 6-L H_2 dose on clean Pt(100) and on a $c(2\times2)$-Ti/Pt(100) surface alloy. According to Norton *et al.*,[23] H_2 adsorption on Pt(100) depends strongly on the surface temperature and H_2 pressure, with θ_H reaching 1.20 ML at 150 K and $P_{H2}\leqslant4.5\times10^{-8}$ Torr. Thus, under the conditions of our experiment, we assume a saturation coverage of $\theta_H=1.20$ ML. The H_2 desorption peak maximum shifted down by 148 K on the alloy compared to that on pure Pt(100), i.e.,

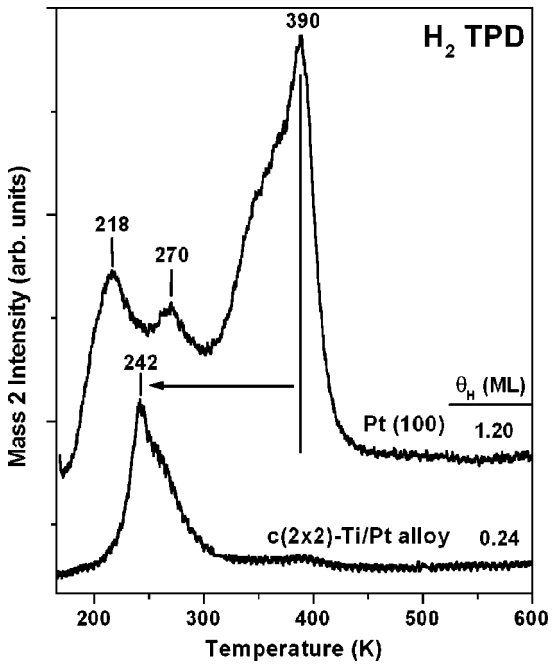

FIG. 12. H_2 TPD curves after a 6-L H_2 dose on a clean Pt(100) surface (top) and on a $c(2\times2)$-Ti/Pt(100) surface alloy (bottom). Much less (20%) hydrogen adsorbed on the alloy and the H_2 desorption activation energy was reduced by 9.3 kcal/mol from that on Pt(100).

from 390 to 242 K. Using Redhead[31] analysis, we calculate that the desorption energy of the highest temperature peak is reduced by 9.3 kcal/mol on the alloy (14.6 kcal/mol) compared to that on the pure Pt(100) surface (23.9 kcal/mol) and nearly 80% less hydrogen desorbed from the $c(2\times2)$-Ti/Pt(100) surface. This may be explained by a filled Pt-*d* band which shifts to higher binding energy with respect to the fermi level upon alloying.[22] Hence, using the simple Harris-Anderson concept,[35] filled *d* states increase the Pauli repulsion between the molecule and surface, thereby increasing the dissociation barrier[36] for H_2. Of course, we have no information about the hydrogen binding sites on the alloy, but Zemlyanov[37] *et al.* utilizing HREELS found that at 170 K, hydrogen adsorbed at fourfold hollow sites or bridge sites on (1×1)-Pt(100) and desorbed from the bridge sites at 240–350 K.

The primary desorption peak in Fig. 12 for the $c(2\times2)$-Ti/Pt(100) surface occurs at 242 K. Bardi *et al.*,[38] observed the same phenomenon on a polycrystalline Pt_3Ti surface, where essentially no H_2 was adsorbed at room temperature.

DISCUSSION

Chemical changes are often observed when comparing different types of alloys or different ordered alloys of the same materials.[39–43] Therefore, determining the composition and structure of the $c(2\times2)$-Ti/Pt(100) surface is important in order to understand the chemical behavior of this system. Three real space models can be proposed for the $c(2\times2)$ unit cell that are based on the arrangement of Ti atoms either as an ordered overlayer, surface alloy, or second layer ''subsurface'' alloy. An overlayer model places Ti atoms in fourfold hollow sites on the Pt surface, with a Ti coverage of 0.5 ML. An incorporated $c(2\times2)$ surface alloy model also has a Ti coverage of 0.5 ML, but places Ti atoms in the surface layer replacing Pt atoms at Pt sites. Finally, a second-layer alloy model places 0.5-ML Ti atoms in a $c(2\times2)$ arrangement, very similar to the incorporated model, but Ti atoms are confined to the second layer rather than at the surface, and are covered by a monolayer of pure Pt in a (1×1)-(100) structure.

Using our ALISS and XPD results, we can exclude the Ti adlayer model. In such a case, the enhanced-scattering peak along the [110] azimuth would occur at a much lower angle for the $c(2\times2)$ adlayer compared with the pure (1×1)-Pt(100) surface, because the distance between Ti atoms along that direction would be twice that of the primitive unit cell distance for Pt(100). In ALISS, longer distances between scattering centers leads to enhanced peaks at lower angles in the spectra. In the Sn/Pt(100) system, for example, Li^+-Sn scattering scans along the [110] azimuth had a critical angle of 12.7° for a Sn overlayer compared to 19.1° for an incorporated surface alloy.[26] For the Ti/Pt(100) system, we observed no significant change in the Li^+-Pt peak position along the [110] direction between the Ti/Pt surface and pure Pt [Figs. 9(a) and 9(b)]. Moreover, the enhanced peaks shown in Figs. 9(b) and 9(c) for both Pt and Ti scattering on the $c(2\times2)$-Ti/Pt(100) alloy occur at the same critical angle along the [110] azimuth. This suggests that Pt and Ti are present in the same plane, therefore excluding an overlayer model. However, ALISS spectra taken along the [110] azimuth cannot distinguish between a Ti/Pt alloy formed within the first layer from one formed within the second layer.

ALISS spectra along the [100] azimuth, combined with XPD results, can be used to determine whether Ti in the Ti/Pt(100) alloy is present in the first or second layer. We should note that ALISS spectra along the [100] azimuth cannot distinguish between a $c(2\times2)$ overlayer and an incorporated surface alloy, however, an overlayer model must be discarded based on the discussion above. Scattering spectra for Ti in the Ti/Pt(100) alloy along the [100] direction in Fig. 10(c) show no enhanced peak at low critical angle as one would expect for Ti atoms present in the surface layer. However, there is a high-angle enhanced peak observed at around 70° due to Ti present in the second layer. Further support for this subsurface Ti model comes from XPD results, where the Ti 2*p* scan [Fig. 7(c)] had an enhanced peak at around 45°, corresponding to Ti located in the second layer. These results are only consistent with an alloy model that places Ti atoms in the second layer of the $c(2\times2)$-Ti/Pt(100) alloy.

Figure 13 shows a model of the $c(2\times2)$-Ti/Pt(100) surface alloy with a pure-Pt surface layer and Ti/Pt(100)-$c(2\times2)$ second layer. While Pt segregation is known to occur in bulk Pt-Ti alloys,[11,22] the formation of a pure-Pt surface layer on top of the second-layer alloy in this system is surprising based on simple thermodynamic arguments usually invoked. For example, Ti has a lower surface free energy than does Pt (1500 mJ/m^2 versus 1860 mJ/m^2), which should favor Ti segregation.[44] Also, Ti metal atoms are larger than those of

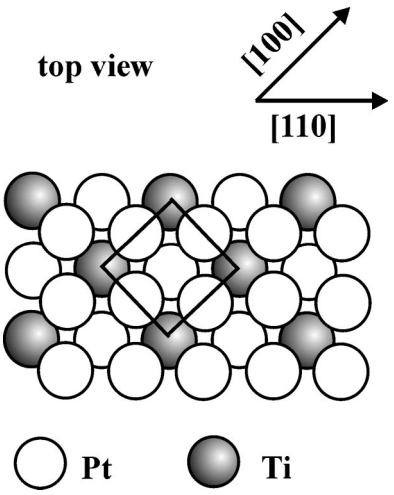

FIG. 13. Schematic drawing of the proposed model for a $c(2\times2)$-Ti/Pt(100) surface alloy. Ti atoms in the figure are shaded gray.

Pt (1.46 Å versus 1.39 Å) and thus strain induced by the atomic-size mismatch should be relieved by Ti segregation to the surface. These factors favor Ti in the surface layer of a Ti-Pt alloy. However, Ti-Pt alloying is strongly exothermic, and interdiffusion into the second layer allows Ti to maximize the number of Pt nearest neighbor atoms. Our results show that strong Ti-Pt intermetallic bonding dominates the surface energetics, leading to Ti atoms located within the second layer, overcoming driving forces from Pt and Ti surface free energies and atomic sizes. Such a phenomenon has also been observed in Ir/Cu(001),[45] Al/Pd(001),[46] and V/Pd(111)[47] systems.

Carbon monoxide TPD results from a clean Pt(100) surface and Ti/Pt(100) alloy reveal additional insight into the effects of alloying Ti and Pt when compared with previous work on similar systems.[32,48] For example, CO desorption from a $c(2\times2)$ and $(3\sqrt{2}\times\sqrt{2})R45°$-Sn/Pt(100) surface alloy and clean Pt(100) were studied previously by Panja and Koel.[32] They found that the desorption temperature of the most strongly bound CO decreased from 520 K on Pt(100) to 402 K on the $c(2\times2)$-Sn/Pt(100) alloy and further to 396 K on the $(3\sqrt{2}\times\sqrt{2})R45°$-Sn/Pt(100) alloy. Alloying of Pt with Sn caused a reduction of 7–8 kcal/mol in the desorption energy of CO on these alloys compared to Pt(100). Alloying of Ti with Pt had a similar effect on CO bonding, and the CO desorption activation energy was reduced by 8.4 kcal/mol on the $c(2\times2)$-Ti/Pt(100) alloy relative to that on the clean Pt(100) surface.

This trend towards lower desorption activation energies for Ti/Pt alloys compared to pure Pt was found by Pick *et al.*[49] in tight-binding calculations of CO adsorbed on Pt(111) and $Pt_3Ti(111)$ surfaces. These calculations found that the CO adsorption energy decreased by 4.6 and 2.3 kcal/mol for Pt sites and Pt-on-Ti sites, respectively, on the alloy surface. No calculations exist for CO adsorption on (100) Pt-Ti alloy surfaces.

Geometric, or ensemble, effects due to alloying refer to changes in the contiguous areal extent of a catalytically active component due to the presence of a second constituent. This effect could clearly play a role in the Sn/Pt(100)-$c(2\times2)$ surface alloy[50] where all pure-Pt, fourfold hollow sites and pure-Pt, twofold bridge sites are absent from the surface alloy compared to the structure of the (1×1)-Pt(100) surface. Similarly, pure-Pt, threefold sites are eliminated at the $(\sqrt{3}\times\sqrt{3})R30°$-Sn/Pt(111) surface, while such sites are present at the surface of the (2×2)-Sn/Pt(111) alloy and clean Pt(111).[27] Electronic, or ligand, effects due to alloying arise from changes in the electronic structure of the catalytic component due to the presence (bonding) of the second constituent which often results in rehybridization of the valence orbitals. For example, H_2 dissociation is facile on Ni(111), however, there is a large energy barrier for H_2 dissociation on NiAl(110).[51] The barrier arises from increased repulsion due to an electronic effect that can be traced to a downshift of the nickel *d* bands in the alloy.[52] Also, Pt sites in a $Cu_3Pt(111)$ alloy surface were found to be more reactive toward H_2 dissociation than those in a Pt(111) surface, and this was attributed to an electronic effect originating from an upshift of the Pt-*d* bands upon alloying.[53,54] Both geometric and electronic effects alter catalytic behavior of alloys from that of the separate component metals, and it is usually impossible to separate the contributions of each to the overall altered chemical behavior.

In a rare system with a clear separation of ligand and ensemble effects, Sellidj *et al.*[55] observed a 40% reduction in the CO adsorption energy for ultrathin (1–3 ML) Pd films deposited on Ta(110) compared to that on bulk Pd(111) surfaces. This system is similar to that in the present study where the chemistry of surface atoms is altered due to an electronic effect induced by atoms only present in subsurface layers. In other related work, evidence for ligand effects on CO adsorption on $Cu_3Pt(111)$ (Ref. 56) was previously proposed based on TPD and UPS. STM has also been used to distinguish between CO adsorbed on Pt/Co(111) surface sites having different chemical environments.[57] Adsorption energies on different types of sites present at surfaces of these alloys depend not only on the in-plane nearest neighbor composition and structure, but also on the identity and distribution of atoms in subsurface layers. Thus, a separation of the influence of ligand and ensemble effects on CO or H_2 adsorption on these surfaces is quite complicated. However, ''subsurface'' alloys such as the $c(2\times2)$-Ti/Pt(100) structure determined here offer an improved model system for further investigation of ''pure'' ligand effects on chemical behavior. Since the surface layer is pure Pt, ensemble effects on the alloy chemistry as classically discussed are removed. Here, we have used a simple Pt-*d* band filling concept to understand decreased H_2 dissociation on the $c(2\times2)$-Ti/Pt(100) alloy, but detail theoretical studies are needed.

Finally, we mention that we have also an ongoing project studying the structure and catalytic behavior of a (2×2)-Ti/Pt(111) alloy. By drawing comparisons between these two alloys, in conjunction with theoretical studies and experimental results from H_2 chemisorption, we expect to gain additional insight into the subtle electronic effects that influence reactions due to alloying.

CONCLUSIONS

We investigated the structure and chemical behavior of a $c(2\times2)$-Ti/Pt(100) surface alloy using a variety of surface-analytical techniques. Depositing an ultrathin layer of Ti and immediately annealing the surface to 920 K forms a $c(2\times2)$ LEED pattern. Using XPD and ALISS, we show that this structure is due to a $c(2\times2)$ Pt-Ti alloy confined to the second layer with a pure-Pt, (1×1)-Pt(100) monolayer at the surface. CO adsorbed reversibly in a broad peak from this alloy surface in a peak at 376 K. This peak was shifted lower by 132 K from that at 508 K from clean Pt(100). H_2 desorption was also shifted to lower temperatures. In addition, 80% less hydrogen adsorbed on the Pt-Ti alloy surface. These changes in the chemisorption behavior of the Pt-Ti alloy compared to the clean Pt surface can be rather cleanly assigned to an electronic, or ligand, effect induced by strong intermetallic bonding between second-layer Ti atoms and surface Pt atoms. Alloying with Ti reduces the reactivity of Pt for adsorbing CO and H_2.

ACKNOWLEDGMENTS

This material is based upon work supported by the National Science Foundation under Grant No. CHE-0213583. We thank Dr. David Beck for a critical reading of the manuscript.

*Present address: Department of Physics, Tulane University, New Orleans, LA 70118.

†Corresponding author. Fax: +1-213-740-3972. Email address: koel@usc.edu

[1] G. L. Haller, Adv. Catal. **36**, 173 (1989).
[2] S. J. Tauster, S. C. Fung, and R. L. Garten, J. Am. Chem. Soc. **100**, 170 (1978).
[3] R. A. Demmin, C. S. Ko, and R. J. Gorte, J. Phys. Chem. **89**, 1151 (1985).
[4] B. C. Beard and P. N. Ross, J. Phys. Chem. **90**, 6811 (1986).
[5] P. J. Meschter and W. L. Worrell, Metall. Trans. A **7**, 299 (1976).
[6] L. Brewer, *Phase Stability in Metals and Alloys* (McGraw-Hill, New York, 1967).
[7] U. Bardi and P. N. Ross, Surf. Sci. **146**, L555 (1984).
[8] U. Bardi, P. N. Ross, and G. Rovida, Surf. Sci. Lett. **205**, L798 (1988).
[9] U. Bardi, D. Dahlgren, and P. N. Ross, J. Catal. **100**, 196 (1986).
[10] A. Atrei, L. Pedocchi, U. Bardi, G. Rovida, M. Torrini, and E. Zanazzi, Surf. Sci. **261**, 64 (1992).
[11] W. Chen, J. A. K. Paul, A. Barbieri, M. Van Hove, S. Cameron, and D. J. Dwyer, J. Phys.: Condens. Matter **5**, 4585 (1993).
[12] J. Paul, S. D. Cameron, D. J. Dwyer, and F. M. Hoffmann, Surf. Sci. **177**, 121 (1986).
[13] S. D. Cameron and D. J. Dwyer, Surf. Sci. **176**, L857 (1986).
[14] S. Ringler, E. Janin, M. Boutonnet-Kizling, and M. Gothelid, Appl. Surf. Sci. **162–163**, 190 (2000).
[15] D. Beck, M. Batzill, C. Baur, J. Kim, and B. E. Koel, Rev. Sci. Instrum. **73**, 1267 (2002).
[16] F. Mugele, C. Kloos, and P. Leiderer, Rev. Sci. Instrum. **67**, 2557 (1996).
[17] C.-S. Ho, S. Banerjee, B. E. Koel, O. B. Duchemin, and J. E. Polk, Appl. Surf. Sci. (to be published).
[18] T. Matsumoto, S. Hsieh, M. Batzill, and B. E. Koel, Surf. Sci. (to be published).
[19] O. Dulub, W. Hebenstreit, and U. Diebold, Phys. Rev. Lett. **84**, 3646 (2000).
[20] D. E. Beck, M. Batzill, and B. E. Koel (unpublished).
[21] H. Brune, H. Roder, K. Bromann, K. Kern, J. Jacobsen, P. Stoltze, K. Jacobsen, and J. Norskov, Surf. Sci. **349**, L115 (1996).
[22] W. Chen, L. Severin, M. Gothelid, M. Hammar, S. Cameron, and J. Paul, Phys. Rev. B **50**, 5620 (1994).
[23] P. R. Norton, J. A. Davies, D. K. Creber, C. W. Sitter, and T. E. Jackman, Surf. Sci. **108**, 205 (1981).
[24] Y. D. Li, M. R. Voss, N. Swami, Y.-L. Tsai, and B. E. Koel, Phys. Rev. B **56**, 15 982 (1997).
[25] Y.-S. Ku and S. H. Overbury, Surf. Sci. **273**, 341 (1992).
[26] Y. D. Li and B. E. Koel, Surf. Sci. **330**, 193 (1995).
[27] S. H. Overbury, D. R. Mullins, M. T. Paffet, and B. E. Koel, Surf. Sci. **254**, 45 (1991).
[28] C.-S. Ho, S. Banerjee, and B. E. Koel, Phys. Rev. B (to be published).
[29] H. Niehus and G. Comsa, Surf. Sci. **152/153**, 93 (1985).
[30] H. Niehus, J. Vac. Sci. Technol. A **5**, 751 (1987).
[31] P. Redhead, Vacuum **12**, 203 (1962).
[32] C. Panja and B. E. Koel, Isr. J. Chem. **38**, 365 (1998).
[33] P. A. Thiel, R. J. Behm, P. R. Norton, and G. Ertl, J. Chem. Phys. **78**, 7448 (1983).
[34] M. A. Barteau, E. I. Ko, and R. J. Madix, Surf. Sci. **102**, 99 (1981).
[35] J. Harris and S. Andersson, Phys. Rev. Lett. **55**, 1583 (1985).
[36] N. Memmel, Surf. Sci. Rep. **32**, 91 (1998).
[37] D. Y. Zemlyanov, M. Y. Smirnov, and V. V. Gorodeskii, Catal. Lett. **43**, 181 (1997).
[38] U. Bardi, G. A. Somorjai, and P. N. Ross, J. Catal. **85**, 272 (1984).
[39] J. W. Peck and B. E. Koel, J. Am. Chem. Soc. **118**, 2708 (1996).
[40] Y. L. Tsai, C. Xu, and B. E. Koel, Surf. Sci. **385**, 37 (1997).
[41] C. Xu and B. E. Koel, J. Chem. Phys. **100**, 664 (1994).
[42] C. Xu and B. E. Koel, Surf. Sci. **327**, 38 (1995).
[43] C. Panja and B. E. Koel, J. Phys. Chem. A **104**, 2486 (2000).
[44] A. R. Miedema, Z. Metallkd. **69**, 287 (1977).
[45] S. Heinze, R. Abt, S. Blugel, G. Gilarowski, and H. Niehus, Phys. Rev. Lett. **83**, 4808 (1999).
[46] Y. G. Shen, D. J. O'Conner, and J. Yao, Appl. Surf. Sci. **125**, 300 (1998).
[47] C. Konvicka, Y. Jeanvoine, E. Lundgren, G. Kresse, M. Schmid, J. Hafner, and P. Varga, Surf. Sci. **463**, 199 (2000).
[48] M. A. Barteau, E. I. KO, and R. J. Madix, Surf. Sci. **102**, 99 (1981).
[49] S. Pick, J. Phys.: Condens. Matter **9**, 141 (1997).
[50] C. Panja, N. A. Saliba, and B. E. Koel, J. Phys. Chem. B **105**, 3786 (2001).
[51] M. Beutl, K. D. Rendulic, and G. R. Castro, J. Chem. Soc., Faraday Trans. **91**, 3639 (1995).
[52] B. Hammer and M. Scheffler, Phys. Rev. Lett. **74**, 3487 (1995).

[53] B. Hammer and J. K. Norskov, Surf. Sci. **343**, 211 (1995).
[54] B. Hammer and J. K. Norskov, Surf. Sci. **359**, 306 (1996).
[55] A. Sellidge and B. E. Koel, Surf. Sci. **284**, 139 (1993).
[56] U. Schneider, G. R. Castro, and K. Wandelt, Surf. Sci. **287–288**, 146 (1993).
[57] Y. Gauthier, M. Schmid, S. Padovani, E. Lundgren, V. Bus, G. Kresse, J. Redinger, and P. Varga, Phys. Rev. Lett. **87**, 036103 (2001).